Flow structures and kinetic-potential exchange in forced rotating stratified turbulence

Tianyi Li,[1] Minping Wan ◉,[2,*] Jianchun Wang,[2] and Shiyi Chen[1,2,†]

[1]*State Key Laboratory for Turbulence and Complex Systems, College of Engineering, Peking University, Beijing 100871, People's Republic of China*
[2]*Guangdong Provincial Key Laboratory of Turbulence Research and Applications, Department of Mechanics and Aerospace Engineering, Southern University of Science and Technology, Shenzhen, Guangdong 518055, People's Republic of China*

We investigate the long-time evolution of flow structures and the kinetic-potential energy exchange in rotating stratified turbulence, which is of great significance in geophysical flows. Numerical simulations of forced three-dimensional homogeneous rotating stratified turbulence in transient state with different Froude numbers are performed. Numerous small vortices spread in the flow, besides a cyclone and an anticyclone that fill up the domain after a very long time. Cyclonic vortices, though being less numerous than anticyclonic vortices, grow faster, thus becoming comparable to the domain scale at an earlier time. When the strength of stratification is varied, we find that in the case with weak stratification, the intensity of global kinetic-potential energy exchange is nearly constant in earlier times, while it oscillates in time at later times. Moreover, for the simulation with weak stratification, the areas of intense kinetic-potential energy exchange tend to concentrate in segmented cylinders. In contrasts, when the strength of stratification is comparable to that of rotation, the areas of intense kinetic-potential energy exchange populate the flow as quadrupoles. For both simulations with stratification, the intense kinetic-potential energy exchange is found to be associated with the cyclonic structures. A possible relation between the sign of ω_z and the spatial distribution of the density field θ is proposed, and the conditional average $\langle \partial \theta / \partial z | \omega_z \rangle$ is found to be almost time-invariant throughout most of the domain.

I. INTRODUCTION

Turbulence subjected to rotation and stratification is of crucial importance for us to understand the physics which is widespread in geophysical flows such as atmospheric and oceanic turbulence [1,2]. For a fluid under rotation and stratification, the Coriolis and buoyancy forces are introduced into the momentum equation in addition to the nonlinear term. Besides the Reynolds number Re, there are two more dimensionless numbers controlling the flow, namely, the Rossby number Ro and the Froude number Fr, representing the relative strength of the inertial term to the Coriolis force and the buoyancy force, respectively.

Previous studies on rotating and/or stratified turbulence have mainly focused on the energy spectrum to elucidate the natural occurrences in the ocean and in the atmosphere [3–9]. In addition, extensive research has been conducted to investigate the energy transfer in rotating and/or stratified turbulence to shed more light on the underlying physics. Normal-mode decomposition has been

---

*wanmp@sustech.edu.cn
†chensy@sustech.edu.cn

adopted widely to decompose the flow field into the wave and potential vorticity (PV) components [10]. There are many other studies investigating the energy transfer between different normal modes [11–15].

As for purely rotating turbulence without stratification [16–19], a series of studies has shown that when Ro is small enough there exists an inverse energy cascade, and the energy in spectral space tends to concentrate in the wave number plane normal to the rotation axis, resulting in a quasi-two-dimensional (quasi-2D) flow [20–22]. Waleffe used an "instability assumption" [23] of the triadic energy transfers to provide a simple argument for the aforementioned trend to be two-dimensionalized in rotating turbulence [24]. Chen *et al.* [25] examined the predictions of the wave resonance theory numerically at a fixed Reynolds number with different Rossby numbers. Their results verified that the resonant interactions of slow modes are important to the inverse energy cascade in three-dimensional (3D) rotating turbulence.

For purely stratified turbulence without rotation [26–28], Godeferd and Cambon [29] adopted an eddy-damped quasinormal Markovian (EDQNM) closure with the axisymmetry hypothesis to analyze the anisotropic energy transfers. For Fr smaller than a critical value of $O(1)$, energy is transferred to large scales when the integration time is sufficiently long [12]. Waite and Bartello [30] used numerical simulations to demonstrate the lack of an inverse cascade of vortical energy and that the transfer of vortical energy to wave energy occurs most efficiently at a vertical scale of U/N, where U is a characteristic horizontal velocity and N is the Brunt-Väisälä frequency.

With regard to rotating stratified turbulence [31–35], Bartello [36] investigated the properties of the energy cascade in rotational and wave modes using both numerical and analytical methods. Using the rapid distortion theory (RDT) to acquire the linear solutions of such systems, Hanazaki [37] showed that the phase of the energy/flux oscillation and the energy distribution among different components are determined by the ratio f/N. Marino *et al.* [38] found a faster growth of kinetic energy in large scales for $1/2 \leqslant N/f \leqslant 2$.

The evolution of flow structures in rotating stratified turbulence is one of our major interests in this paper. For purely rotating turbulence, Bartello *et al.* [20] investigated the formation and stability of quasi-2D coherent vortices. They showed that, at small rotation rate (Ro $\sim$ 1), the rotation destabilizes anticyclones, while cyclonic vortices can still exist. At a larger rotation rate (Ro $\ll$ 1), they showed the emergence of both 2D cyclones and anticyclones, consistent with the Taylor-Proudman theorem. As for rotating stratified turbulence, McWilliams *et al.* [39] performed numerical simulations of unforced quasi-geostrophic (QG) equations for a Boussinesq fluid with uniform rotation and stable stratification. They demonstrated that the flow evolves into a system with a large population of coherent vortices, and their chaotic interactions dominate the subsequent evolution of the flow. For quasi-geostrophic flows, Reinaud and Dritschel [40] studied different regimes of the interaction between two vertically offset vortices, and Reinaud *et al.* [41] displayed that the population of vortices exhibits a mean height-to-width aspect ratio close to f/N. Cambon [42] showed that the anisotropic spectral description, including the angular dependence of spectra and cospectra in Fourier space, is relevant to quantify "columnar" and "pancake" structures in physical space. Smith and Waleffe [12] examined the flow structures using the contour levels of the zonal velocity for varying degrees of stratification and rotation. They pointed out that the slow large scales consist of vertically sheared horizontal flow for strongly stratified flows. Liechtenstein *et al.* [43] investigated constant enstrophy surfaces for turbulence with different stratification and rotations to illustrate the flow structures under different conditions.

Kinetic-potential energy exchange is one of the important turbulent quantities in rotating stratified turbulence. In the present paper, kinetic-potential energy exchange and its connection with flow structures are investigated in detail. Buoyancy flux (proportional to the kinetic-potential energy exchange) has been widely studied in purely stratified turbulence [44–46]. For rotating stratified turbulence, Ramsden and Holloway [47] showed that the imbalance between the transfer efficiencies of kinetic energy (KE) and potential energy (PE) from large to small scales causes the buoyancy flux to be negative (KE to PE) at large scales and positive (PE to KE) at small scales. They also showed that the results related to buoyancy flux are sensitive to the form of energetic forcing. Hanazaki [37]

analyzed kinetic and potential energies and the vertical density flux using RDT. Comparison with previous numerical and experimental results showed that the linear processes of RDT can explain many unsteady aspects of these quantities. Furthermore, kinetic-potential energy exchange is closely relevant to inertia-gravity waves, which are important to the breakdown of balance that is discussed in many recent studies [48–50].

The remainder of this paper is organized as follows. In Sec. II we introduce the numerical setup of our simulations. The results of flow structures obtained from the numerical simulations are shown in Sec. III. In Sec. IV we present the structures of the kinetic-potential energy exchange and their relevance to flow structures. The connection between the density distribution and the velocity are discussed in Sec. V. Finally, our conclusions are summarized in Sec. VI.

II. NUMERICAL SETUP

The Boussinesq equations to be integrated numerically are written as below:

$$\frac{D\boldsymbol{u}}{Dt} + f\hat{z} \times \boldsymbol{u} + N\theta\hat{z} + \frac{1}{\rho_0}\boldsymbol{\nabla}p = \nu\nabla^2\boldsymbol{u} + \boldsymbol{F}_u, \tag{1}$$

$$\frac{D\theta}{Dt} - N(\boldsymbol{u}\cdot\hat{z}) = \kappa\nabla^2\theta, \tag{2}$$

$$\boldsymbol{\nabla}\cdot\boldsymbol{u} = 0, \tag{3}$$

where $D/Dt = \partial/\partial t + \boldsymbol{u}\cdot\boldsymbol{\nabla}$ is the material derivative, $\boldsymbol{u}$ is the Eulerian velocity, f is twice the frame rotation rate Ω, ρ_0 is the reference density from the Boussinesq approximation, p is the effective pressure consisting of a normal pressure and a centrifugal term $p = p_0 + \frac{1}{2}\rho\|\boldsymbol{\Omega}\times\boldsymbol{x}\|^2$, $\boldsymbol{\Omega} = \Omega\hat{z}$ is the rotation vector, ν is the kinematic viscosity, and κ is the diffusion coefficient. We decomposed the total density ρ as

$$\rho = \rho_0 - cz + \rho',\, \rho' = \left(\frac{c\rho_0}{g}\right)^{1/2}\theta, \tag{4}$$

where c is a positive constant for a uniform stable stratification, $\rho_0 - cz$ is the density field of a hydrostatic state, ρ' is a small density fluctuation field, g is the gravitational acceleration. θ is rescaled from ρ' to have a dimension of velocity. $N = (gc/\rho_0)^{1/2}$ is the buoyancy (Brunt-Väisälä) frequency. The term $\boldsymbol{F}_u$ represents external forcing of the velocity. Do note that there is no direct external forcing in the density fluctuations θ.

We performed direct numerical simulations (DNS) of Eqs. (1)–(3) using a parallelized pseudospectral code in a 256^3 periodic box with a Gaussian forcing spectrum such that the spectral injection rate is $\epsilon(k) = \sum_{|\boldsymbol{k}|=k}\sum_i\epsilon_i(\boldsymbol{k})$ with standard deviation $s = 1$ and energy input rate $\epsilon_f = 1$, given by

$$\epsilon(k) = \epsilon_f\frac{\exp[-0.5(k - k_f)^2/s^2]}{(2\pi)^{1/2}s}. \tag{5}$$

The forcing in Eq. (1) is

$$F_{u,i}(\boldsymbol{k}, t) = \epsilon_i(\boldsymbol{k})/\hat{u}_i(\boldsymbol{k}, t)^*, \tag{6}$$

generating a kinetic energy input $\epsilon_i(\boldsymbol{k})$ at the wave number $\boldsymbol{k}$ and time t. $\epsilon_i(\boldsymbol{k})$ are identical in all directions (which are indicated by i). Here $\hat{u}_i(\boldsymbol{k}, t)^*$ represents the conjugate of Fourier component $\hat{u}_i(\boldsymbol{k}, t)$. Froude and Rossby numbers are defined based on the forcing parameters, as

$$\mathrm{Fr} = \frac{\left(\epsilon_f k_f^2\right)^{1/3}}{N}, \quad \mathrm{Ro} = \frac{\left(\epsilon_f k_f^2\right)^{1/3}}{f}. \tag{7}$$

For all the simulations, the Froude number is varied by modifying N, while the Rossby number and forcing parameters remain unchanged.

TABLE I. Simulation parameters: n_p is the linear grid resolution, k_f the forcing wave number, $\text{Re}_{(q)}$ the Reynolds number based on hyperviscosity, Ro the Rossby number, Fr the Froude number (Fr $= \infty$ indicates the purely rotating case), $\text{Re}_{b,(q)}$ the buoyancy Reynolds number, t_e the overall integration time, and τ_0 the initial large-eddy turnover time.

Run	n_p	k_f	$\text{Re}_{(q)}$	Ro	Fr	$\text{Re}_{b,(q)}$	t_e
1	256	45	2100	0.033	∞	∞	$496\tau_0$
2	256	45	2100	0.033	0.42	368	$496\tau_0$
3	256	45	2100	0.033	0.052	6	$496\tau_0$

To extend the inertial range, we replaced the normal viscosity term $\nu\nabla^2\boldsymbol{u}$ with a hyperviscosity term $(-1)^{q+1}\nu_q(\nabla)^{2q}\boldsymbol{u}$ with $q = 8$. The diffusion term in Eq. (2) is replaced in a similar way by $(-1)^{q+1}\kappa_q(\nabla)^{2q}\theta$. The Reynolds number based on hyperviscosity $\text{Re}_{(q)} = \epsilon_f^{1/3}/(\nu_q k_f^{2(q-1/3)})$ is held fixed at around 2100 and the Prandtl number $\text{Pr} = \nu_q/\kappa_q$ remains unity for all the simulations. The corresponding buoyancy Reynolds number is defined by $\text{Re}_{b,(q)} = \text{Re}_{(q)}\text{Fr}^2 = \epsilon_f/(\nu_q k_f^{2(q-1)}N^2)$. For more detailed information regarding the specific procedures of the code, please refer to Ref. [12].

We use homogeneous isotropic turbulence as the initial condition and initialize the buoyancy field with $\theta = 0$ everywhere in the domain. Rotation and stratification are introduced at the beginning of the simulation. Simulations with different initial conditions have been performed and show that our conclusions are reproducible and universal. We use an intermediate forcing wave number k_f and focus on the dynamics in the inverse energy cascade range $k < k_f$ during the transient flow state in this paper. This setup might be useful to understand many phenomena in the atmosphere and oceans. However, since the atmosphere is never 3D isotropic at the synoptic scales (similarly for the oceans), such a transition does not happen in the atmosphere and oceans. Therefore, readers should be cautious with the applicability of this study to atmospheric or oceanic regimes.

To investigate the effects of stratification on the flow structures and kinetic-potential energy exchange in rotating stratified turbulence, three simulation cases are carried out with the same Rossby number Ro $= 0.033$, but with different Froude numbers Fr $= \infty$ (purely rotating case), Fr $= 0.42$, and Fr $= 0.052$. Parameters of the simulations are given in Table I. Chen $et\ al.$ [25] have shown that when Ro $= 0.033$, the rotation is rapid enough to make the turbulence two-dimensionalized due to resonant interactions. For forced stratified turbulence, sufficiently long integration time is important to the generation of slow large scales [12]. A 256^3 grid was adopted to carry out long-time integrations and a grid independence study was conducted using two different grid sizes (128^3 and 256^3), where further refinement of the 128^3 grid does not have a significant effect on the results. Note that although the Reynolds number $\text{Re}_{(q)}$ is large, the resolution is moderate that Zeman scale and Ozmidov scale are not resolved by the simulations.

III. FLOW STRUCTURES

In this section, the evolutions of flow structures in the simulations are investigated. The classical Q criterion is chosen to identify the flow structures and its threshold is set through the percolation analysis [51]. Using other methods for the identification of flow structures, e.g., dissipation and enstrophy, yield similar results as using Q criterion [52]. The Q criterion defines vortices as connected fluid regions with positive second invariants of the velocity gradient tensor, $Q = \frac{1}{2}[|\boldsymbol{\Omega}|^2 - |\boldsymbol{S}|^2] > 0$, where $\boldsymbol{S} = \frac{1}{2}[\nabla\boldsymbol{u} + (\nabla\boldsymbol{u})^T]$ is the rate-of-strain tensor and $\boldsymbol{\Omega} = \frac{1}{2}[\nabla\boldsymbol{u} - (\nabla\boldsymbol{u})^T]$ is the vorticity tensor. Since Q is proportional to the difference between magnitudes of vorticity and shear strain rate, regions with $Q > 0$ and $Q < 0$ are vortex dominated and strain dominated, respectively. Figure 1 shows the percolation diagram of Q criterion for Run 3 at $t = 480\tau_0$. The percolation results at different times for both Run 2 and Run 3 are similar. The solid line represents the volume of the largest identified object, V_{lar}, normalized with the total volume V_{tot} satisfying $Q > Q_{\text{thres}}$, and
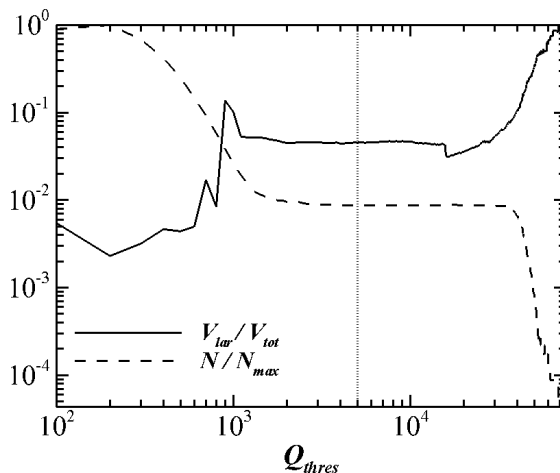
FIG. 1. Percolation diagram for the identification of Q criterion for Run 3 with Ro $= 0.033$ and Fr $= 0.052$ at $t = 480\tau_0$. Solid, ratio of the volume of the largest identified object to the volume of all identified objects, $V_{\text{lar}}/V_{\text{tot}}$; dashed, ratio of the number of identified objects to the maximum number of objects, N/N_{max}. The vertical dotted line indicates the chosen threshold, $Q_{\text{thres}} = 6000$.

the dashed line is the ratio of total number of identified objects, N, to its maximums. The vertical dashed line shows the threshold used in the present work, $Q_{\text{thres}} = 6000$, where $V_{\text{lar}}/V_{\text{tot}}$ and N/N_{max} are nearly constant.

Figure 2 displays the evolution of isosurfaces of Q criterion color-coded with vertical vorticity ω_z for all the simulations. For Run 1 under pure rotation, slender 2D vortices are formed at $t = 40\tau_0$ [see Fig. 2(a)]. These structures remained two-dimensionalized and merged into larger ones continuously [Fig. 2(b)], which agrees with the inverse cascade of kinetic energy from the small scales to large scales [21,53,54]. Both cyclonic and anticyclonic vortices are present in the flow, which is consistent with the observations in Chen *et al.* [25]. An obvious cyclone-anticyclone asymmetry [55–57] dominated by the 2D long-lived cyclones can be seen in Figs. 2(a) and 2(b), echoing the results in Ref. [58]. Whereas at $t = 480\tau_0$, the numbers of cyclones and anticyclones are nearly equal [Fig. 2(c)], indicating the existence of an approximate cyclone-anticyclone symmetry.

For Run 2 with weak stratification, many short vertical vortices can be seen shortly after the simulation started [Fig. 2(d)], which are very likely to be a manifestation of the vortex mode in physical space, since they do not exist in the purely rotating turbulence [43]. At this time, the small amount of box-scale vortices are all cyclonic, while the short vortices have both cyclonic and anticyclonic types. The number of short cyclonic vortices decreases while the number of box-scale cyclonic vortices increases at $t = 240\tau_0$. It is speculated that the box-scale vortices might be formed through the alignment of the short vortices. At this moment, there is not any box-scale anticyclonic vortex, but some short anticyclonic vortices lined up to form box-scale structures [Fig. 2(e)]. At $t = 480\tau_0$, a large box-scale anticyclonic vortex structure is formed through the merging of short anticyclonic vortices, while the largest box-scale cyclonic vortex structure is formed through the merging of the box-scale cyclonic vortices. There are only a small number of short cyclonic vortices, while there are a significant amount of short anticyclonic vortices at this moment [see Fig. 2(f)]. We will discuss the differences between the observed cyclonic and anticyclonic vortices in Sec. V.

For Run 3 with strong stratification, there are numerous short and small vortices spreading over the whole domain at $t = 40\tau_0$ [Fig. 2(g)]. As the turbulent system evolves, cyclonic vortices become longer (by growing or merging) and tend to line up to form a box-scale vortex structure with their shapes becoming more complex, while anticyclonic vortices just become larger and have more complex shapes [Fig. 2(h)]. After a longtime evolution, a second box-scale vortex
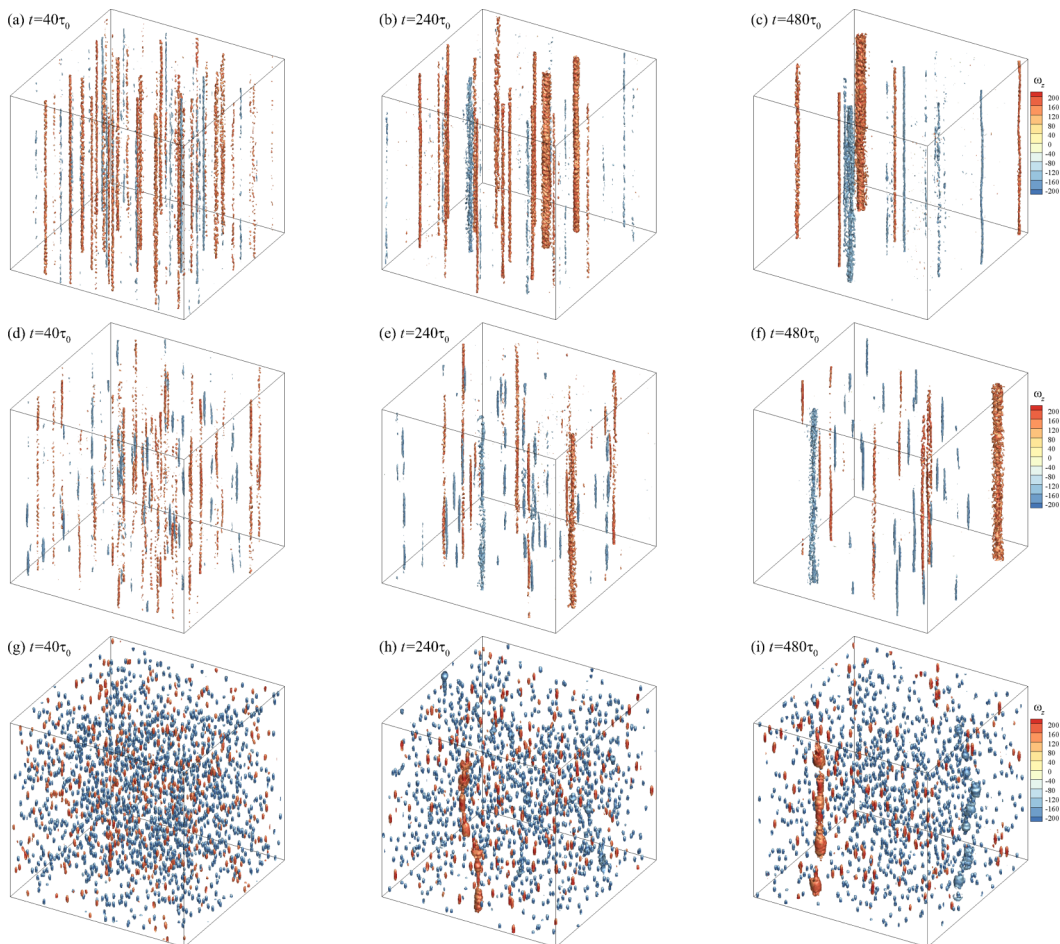
FIG. 2. The evolution of isosurfaces of Q (for $Q = 6000$) color-coded with vertical vorticity ω_z for (a), (b), and (c) Run 1, (d), (e), and (f) Run 2, and (g), (h), and (i) Run 3.

structure is formed through anticyclonic vortices [Fig. 2(i)]. This physical process indicates the transfer of kinetic energy to the large scales, which is consistent with the existence of the inverse cascade in rotating stratified turbulence [11,36,38]. It is found that cyclonic vortices grow faster than anticyclonic ones. Generally, the numbers of the cyclonic vortices are less than anticyclonic vortices, while the volumes of the cyclonic vortices are larger than anticyclonic vortices. Figure 3 gives a quantitative description of the number N_s and the average volume V_m of cyclonic and anticyclonic vortices. They have similar trends for vortices of both types, and the number is less and the average volume is larger for cyclonic vortices when $t > 40\tau_0$. The numbers N_s of vortices of both types are found to first increase rapidly and then slowly decrease, which corresponds to the generation and merging of structures, respectively. However, they remain nearly constant after $t = 200\tau_0$ [Fig. 3(a)]. Meanwhile, the average volumes V_m of vortices of both types become larger at early times, which indicates the growing up or merging of structures. V_m of cyclonic vortices varies around a constant value when $t > 120\tau_0$, and V_m of anticyclonic vortices remains nearly constant when $t > 40\tau_0$.

In this section, we investigated the evolution of flow structures in the purely rotating and rotating stratified turbulence. Vortices get shorter as the strength of stratification increases and most of them exhibits an aspect ratio close to f/N, which is consistent with previous studies [41,59]. Besides the
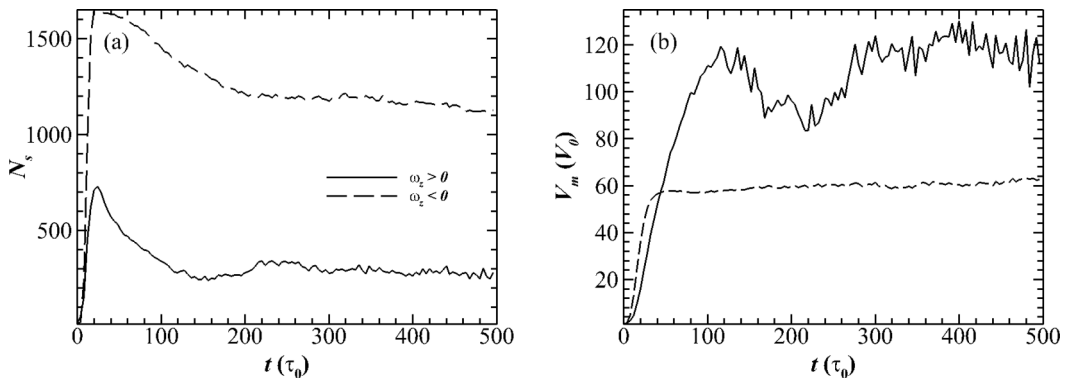
FIG. 3. Time variations of (a) the number N_s and (b) the average volume V_m of cyclonic and anticyclonic vortices in Run 3. Solid, for cyclonic vortices where $\omega_z > 0$; dashed, for anticyclonic vortices where $\omega_z < 0$. V_0 is the volume of a cubic mesh.

sustained forcing and the inverse cascade, the vertical columns observed here might be attributed to poor vertical resolution and diffusion [41]. For both simulations with stratification (Run 2 and Run 3), compared with the anticyclonic vortices (with $\omega_z < 0$), cyclonic vortices (with $\omega_z > 0$) form the largest box-size vortex at a much earlier time. After $t = 40\tau_0$, cyclonic vortices are less in number and have larger average volumes. We will discuss the differences between the two types of vortices in detail in Sec. V. Note that the tracking method in Lozano-Durán and Jiménez [60] can be used to investigate more details of the time evolution of the structures (for example, the advection, generation, vanishing, splitting and merging of structures), which we devote to a future study.

IV. KINETIC-POTENTIAL ENERGY EXCHANGE

Kinetic-potential energy exchange plays a key role in stratified turbulent flows [37]. In this section, we try to find the primary carriers of kinetic-potential energy exchange in rapidly rotating stratified turbulent systems and focus on the relevant coherent structures.

To compare the intensity of global kinetic-potential energy exchange in the simulations with different stratification, we show in Fig. 4 the time evolution of the global kinetic-potential energy exchange, namely, the energy transferred from kinetic energy to potential energy per unit volume,
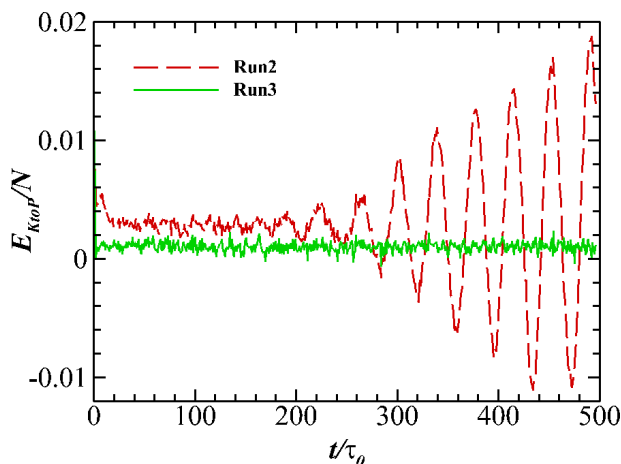

FIG. 4. Time series of the intensity of global kinetic-potential energy exchange for Run 2 and Run 3.

$E_{KtoP} = 1/V \int_D v_z N\theta \, d\boldsymbol{x}$, rescaled by N for Run 2 and Run 3. In regard to kinetic-potential energy exchange, rotation acts as a driving force, since it two-dimensionalizes the flow, imposing vertical displacements on fluid particles during the process of two-dimensionalization, while stable stratification acts as a stabilizing force. Therefore, it is not hard to explain that the intensity of global kinetic-potential transport of Run 2 is stronger than that of Run 3 for $t < 200\tau_0$, because Run 2 has weaker stratification.

For Run 2, there is an interesting observation that the global kinetic-potential energy exchange begins to oscillate after around $200\tau_0$ with an increasing magnitude and a period of $37\tau_0$. Do note that the magnitude will not increase infinitely (not shown). Therefore, two flow states can be identified based on the global kinetic-potential energy exchange at early and late times. Such behavior of the global kinetic-potential energy exchange is reminiscent of many other physical systems subjected to a driving force and a stabilizing force, where an appropriate relative strength of the two forces can make the flow structures more coherent, resulting in a higher efficiency of turbulent transport [61].

A. Rotating turbulence with weak stratification

To investigate the kinetic-potential energy exchange in the physical space, we consider $e_{KtoP}(\boldsymbol{x}, t) = v_z N\theta$, which indicates the instantaneous amount of kinetic energy transferred to potential energy at the spatial position $\boldsymbol{x}$ and time t (negative sign means the opposite direction of transfer). Since the kinetic to potential energy transfer function in spectral space $T_{KtoP}(k_h, k_z)$ concentrates on the $k_z = 0$ plane (not shown), where $k_h = (k_x^2 + k_y^2)^{1/2}$ is the magnitude of horizontal wave number, and the flow structures in physical space are also two-dimensionalized (Sec. III), we vertically average the 3D e_{KtoP} as

$$\bar{e}_{KtoP}^z = \frac{1}{H} \int_0^H e_{KtoP}(x, y, z)dz, \tag{8}$$

with H representing the vertical height of the domain. Figure 5 displays the evolution of $\bar{e}_{KtoP}^z$ for Run 2, normalized by its instantaneous largest absolute value. A large area of oscillating $\bar{e}_{KtoP}^z / |\bar{e}_{KtoP}^z|_{\max}$ with large magnitude is formed after around $t = 200\tau_0$ [Fig. 5(c) and 5(d)], corresponding to the flow state at later times, where the most intense T_{KtoP} oscillates in the 2D plane (where $k_z = 0$) and concentrates around a certain large scale $k_h \approx 10$ (not shown). The magnitude of $\bar{e}_{KtoP}^z$ in most part of the region outside the large area of intense $\bar{e}_{KtoP}^z / |\bar{e}_{KtoP}^z|_{\max}$ is negligible. The overall contribution of the large-scale area of intense $\bar{e}_{KtoP}^z / |\bar{e}_{KtoP}^z|_{\max}$ to the global kinetic-potential energy exchange E_{KtoP} is dominant, indicating that it is the formation of the large-scale area of intense $\bar{e}_{KtoP}^z / |\bar{e}_{KtoP}^z|_{\max}$ that causes the oscillation of the global kinetic-potential energy exchange. Such a dominant area of intense kinetic-potential energy exchange is very likely related to certain coherent structures, which will be discussed later.

Although the flow structures are two-dimensionalized, the structures of kinetic-potential energy exchange e_{KtoP} still have a large-scale variation in vertical direction. In order to study the large-scale information of e_{KtoP}, we use a filtering approach [62] to get a "coarse-grained" field, using a smooth low-pass filter:

$$\bar{\boldsymbol{u}}_l(\boldsymbol{x}) = \int d\boldsymbol{r} G_l(\boldsymbol{r}) \boldsymbol{u}(\boldsymbol{x} + \boldsymbol{r}), \tag{9}$$

where $G_l(\boldsymbol{r}) = l^{-3}G(\boldsymbol{r}/l)$ is a filtering kernel and G is a Gaussian function $G(\boldsymbol{r}) = (6/\pi)^{3/2} \exp(-6r^2)$. So $\bar{\boldsymbol{u}}_l$ only contains information for scales $> l$. Therefore, we can consider the exchange between kinetic and potential energies at large scales, $e_{KtoP,l} = \bar{v}_z N\bar{\theta}$. Figure 6 gives the isosurfaces of e_{KtoP} and $e_{KtoP,l}$ (for $l = 2\pi/5$) at $t = 480\tau_0$, exhibiting the large-scale vertical variation of e_{KtoP} clearly. The structures with intense large-scale kinetic-potential energy exchange $e_{KtoP,l}$ are segmented as two cylinders with positive values and two cylinders with negative values
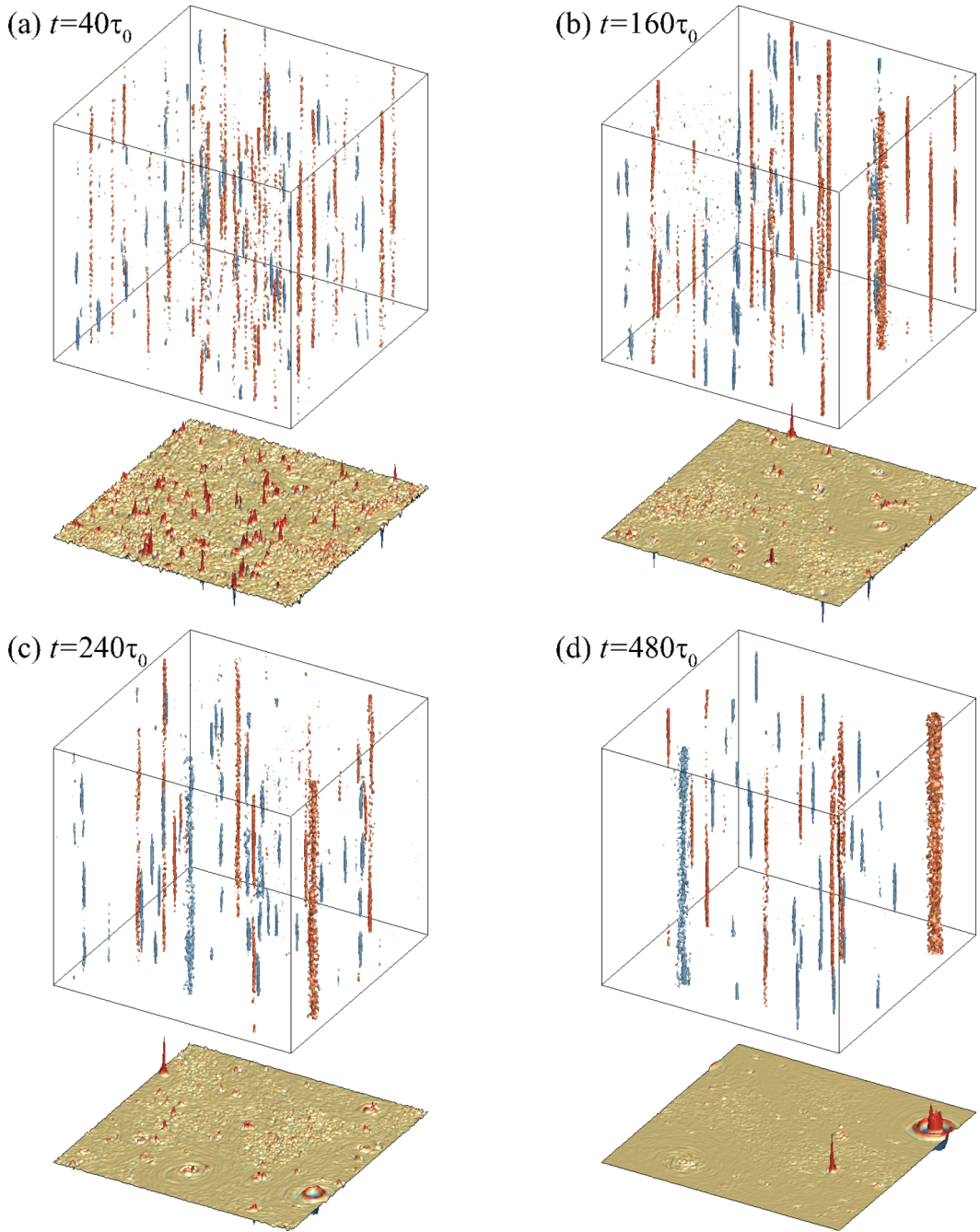
FIG. 5. Isosurfaces of Q color-coded with vertical vorticity ω_z (reddish color represents $\omega_z > 0$ and bluish color represents $\omega_z < 0$) and normalized vertically averaged kinetic-potential energy exchange $\bar{e}^z_{KtoP}/|\bar{e}^z_{KtoP}|_{\max}$ (below) for Run 2 at different times. Note that areas of intense $\bar{e}^z_{KtoP}/|\bar{e}^z_{KtoP}|_{\max}$ are always accompanied with cyclonic vortices.
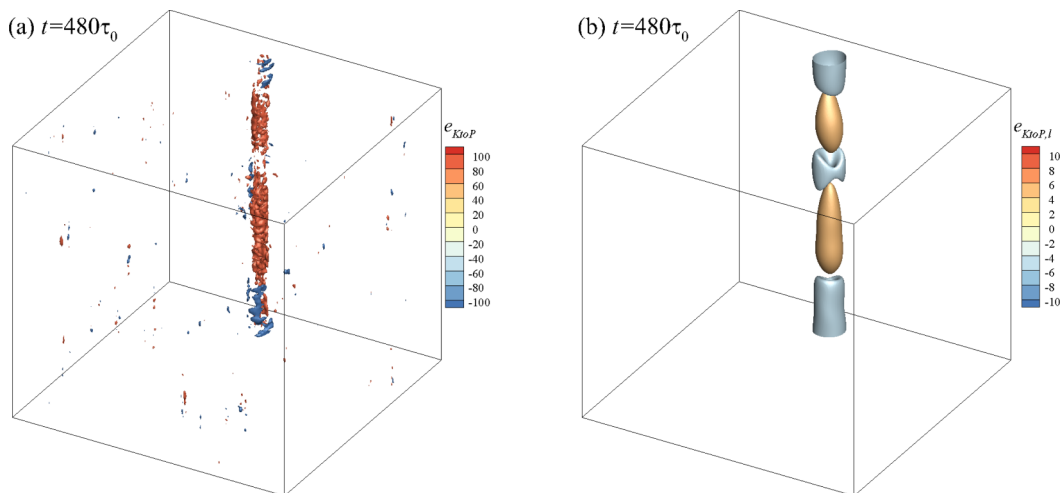
FIG. 6. Isosurfaces of (a) kinetic-potential energy exchange e_{KtoP} (for $e_{KtoP} = \pm 100$) and (b) large-scale kinetic-potential energy exchange $e_{KtoP,l}$ (for $e_{KtoP,l} = \pm 5$) for Run 2 at $480\tau_0$.

(not three parts, because of the periodicity). Note that at $t = 480\tau_0$, the buoyancy length scale $U/N \approx 0.14$, where U is the r.m.s. velocity.

To identify the coherent structures that are responsible for kinetic-potential energy exchange, we plot the isosurfaces of Q (for $Q = 6000$) and normalized vertically averaged kinetic-potential energy exchange $\bar{e}_{KtoP}^z / |\bar{e}_{KtoP}^z|_{\max}$ for Run 2 in Fig. 5. It is remarkable that the areas of intense kinetic-potential energy exchange are associated with cyclonic vortices rather than anticyclonic vortices, especially for the large area of intense $\bar{e}_{KtoP}^z / |\bar{e}_{KtoP}^z|_{\max}$ at $t = 480\tau_0$. Since the turbulence is rotation-dominated, the vertical movement of the fluid particles is induced in the course of the flow to be two-dimensionalized and thus, transferring kinetic energy to potential energy. This process corresponds to the stretching and contracting of vortices. More details about this process will be discussed in Sec. V. A long integration time resulted in a cyclonic vortex condensation, thus changing the global kinetic-potential energy exchange significantly. Condensation of coherent structures also plays a crucial role in the convective heat transfer of turbulent Rayleigh-Bénard convection system [63].

Figures 7(a) and 7(b) give the average of $|e_{KtoP}|$ conditioned on Q and ω_z, $\langle |e_{KtoP}||Q \rangle$ and $\langle |e_{KtoP}||\omega_z \rangle$, normalized by its spatial average in the whole domain, $\langle |e_{KtoP}| \rangle$. It is easy to find

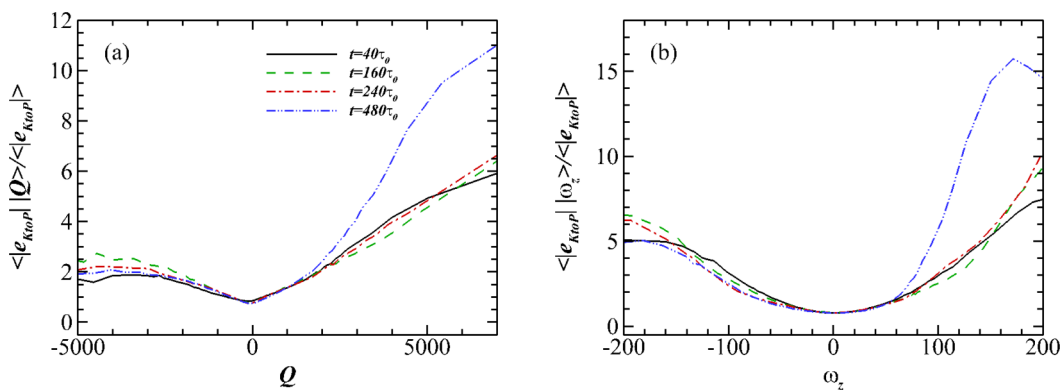
FIG. 7. The average of $|e_{KtoP}|$ conditioned on (a) Q and (b) ω_z, normalized by its spatial average in the whole domain, for Run 2, at different times: $40\tau_0$, black; $160\tau_0$, green; $240\tau_0$, red; $480\tau_0$, blue.
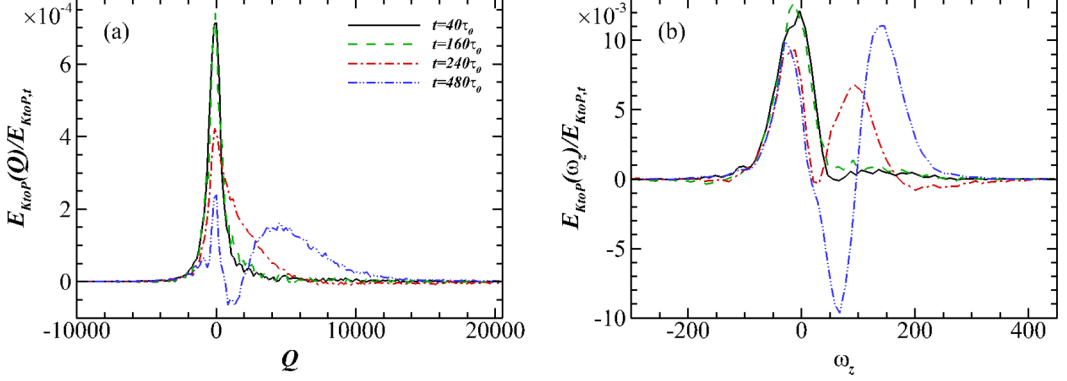
FIG. 8. The contribution fraction to global kinetic-potential energy exchange $E_{KtoP,t}$ (a) from different Q, $E_{KtoP}(Q)/E_{KtoP,t}$, and (b) from different ω_z, $E_{KtoP}(\omega_z)/E_{KtoP,t}$, for Run 2, at different times.

that $|e_{KtoP}|$ is very small when Q is near zero. Moreover, $|e_{KtoP}|$ is more likely to be larger in vortex regions ($Q > 0$) than in strain regions ($Q < 0$). From $t = 40\tau_0$ to $t = 240\tau_0$, the curves do not change significantly with time. However, the conditional average, $\langle|e_{KtoP}||Q\rangle$ is found to increase significantly in vortex regions ($Q > 0$), from $t = 240\tau_0$ to $t = 480\tau_0$. Figure 7(b) shows that $\langle|e_{KtoP}||\omega_z\rangle$ behaves in a similar way as $\langle|e_{KtoP}||Q\rangle$. This is consistent with the observation in Fig. 5 that the areas of intense kinetic-potential energy exchange are always associated with strong cyclonic vortices.

To show the contribution from regions with different values of Q and ω_z to the global kinetic-potential energy exchange $E_{KtoP,t} = \int_D e_{KtoP}(\boldsymbol{x})\,d\boldsymbol{x}$, we defined $E_{KtoP}(\widetilde{Q}) = \int_D \delta(Q(\boldsymbol{x}) - \widetilde{Q})e_{KtoP}(\boldsymbol{x})\,d\boldsymbol{x}$ and $E_{KtoP}(\widetilde{\omega}_z) = \int_D \delta(\omega_z(\boldsymbol{x}) - \widetilde{\omega}_z)e_{KtoP}(\boldsymbol{x})\,d\boldsymbol{x}$, where D represents the whole domain and $\delta(x)$ is the Dirac delta function. Figure 8(a) shows $E_{KtoP}(Q)/E_{KtoP,t}$, representing the contribution fraction to $E_{KtoP,t}$ from regions with different values of Q. For the early flow state ($t < 200\tau_0$) when the global kinetic-potential energy exchange is nearly constant, $E_{KtoP}(Q)/E_{KtoP,t}$ distributes approximately symmetrically around $Q = 0$ and the total $E_{KtoP}(Q)/E_{KtoP,t}$ from strain regions ($Q < 0$) is approximately equal to that from vortex regions ($Q > 0$). At this moment, none of the largest structures is formed. Although the intensity of kinetic-potential energy exchange (indicated by $\langle|e_{KtoP}||Q\rangle/\langle|e_{KtoP}|\rangle$) is large for large positive values of Q (Fig. 7), the contribution mainly comes from the regions where $|Q| < 3000$, because of the cancellation and rarity of areas of intense kinetic-potential energy exchange [Figs. 5(a) and 5(b)]. Moreover, $E_{KtoP}(Q)/E_{KtoP,t}$ is found to be greater than zero for almost all Q. As the turbulent system evolves into the later flow state ($t > 200\tau_0$) with oscillating global kinetic-potential energy exchange, more vortex regions ($Q > 0$) get significant $E_{KtoP}(Q)/E_{KtoP,t}$ and there is a negative $E_{KtoP}(Q)/E_{KtoP,t}$ from $Q = 0$ to $Q = 2000$ at $t = 480\tau_0$. The total $E_{KtoP}(Q)/E_{KtoP,t}$ from strain regions ($Q < 0$) is less when compared to that from vortex regions ($Q > 0$) at $t = 480\tau_0$. This is consistent with the formation of a dominant area of intense kinetic-potential energy exchange associated with a large cyclonic vortex [Fig. 5(d)].

Figure 8(b) shows the contribution fraction to $E_{KtoP,t}$ from different regions with ω_z, $E_{KtoP}(\omega_z)/E_{KtoP,t}$. For the early flow state ($t < 200\tau_0$) when the global kinetic-potential energy exchange is nearly constant, $E_{KtoP}(\omega_z)/E_{KtoP,t}$ distributes approximately symmetrically around a negative value of ω_z and the total $E_{KtoP}(\omega_z)/E_{KtoP,t}$ from the regions with $\omega_z < 0$ is larger than that from the regions with $\omega_z > 0$. Moreover, $E_{KtoP}(\omega_z)/E_{KtoP,t}$ concentrates in the regions where $-150 < \omega_z < 100$, and it is almost all positive in these regions. As the turbulent system evolves into the other flow state ($t > 200\tau_0$) with oscillating global kinetic-potential energy exchange, there are more $\omega_z > 0$ regions with significant $E_{KtoP}(\omega_z)/E_{KtoP,t}$ at $t = 240\tau_0$, consistent with the emergence of the areas of intense kinetic-potential energy exchange accompanied with cyclonic vortices.
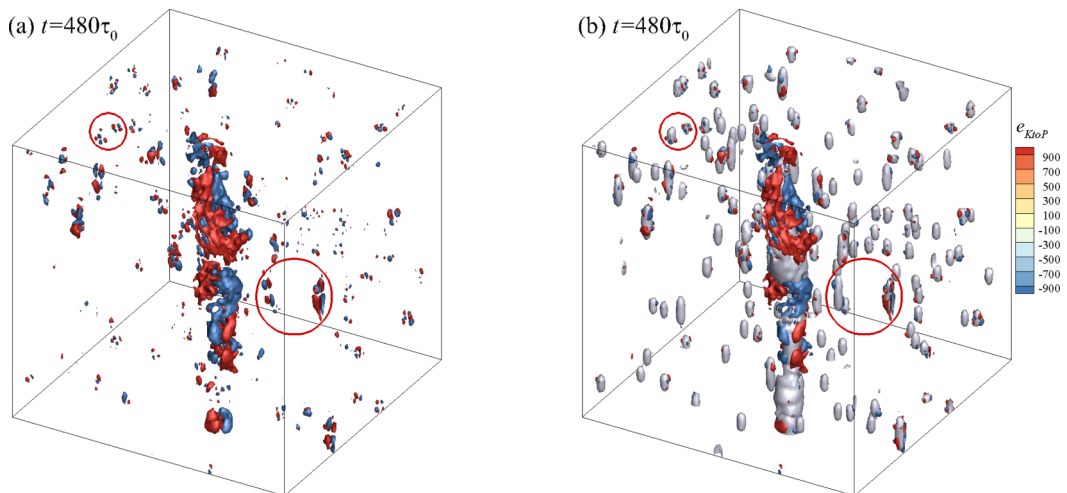
FIG. 9. Isosurfaces of kinetic-potential energy exchange e_{KtoP} (for $e_{KtoP} = \pm1000$) (a) without and (b) with isosurfaces of Q (for $Q = 6000$), for Run 3, at $t = 480\tau_0$. Typical quadrupolar structures around small vortices are circled.

Moreover, the area with ω_z from around 0 to 100 has negative $E_{KtoP}(\omega_z)/E_{KtoP,t}$ at $t = 480\tau_0$. The total $E_{KtoP}(\omega_z)/E_{KtoP,t}$ from the regions with $\omega_z < 0$ is approximately equal to that from the regions with $\omega_z > 0$ at $t = 480\tau_0$.

B. Rotating turbulence with strong stratification

The isosurfaces of kinetic-potential energy exchange, e_{KtoP}, in a 128^3 subdomain of the entire 256^3 domain at $t = 480\tau_0$ is shown in Figs. 9(a) and 9(b) for Run 3 without and with the isosurfaces of Q, respectively. Comparing Figs. 9(a) and 9(b), we can observe that e_{KtoP} has "quadrupolar" structures around the vortices (by Q criterion). For the two largest structures, we can also show that e_{KtoP} around them has "quadrupolar" structures. Figure 10(a) gives the vertically averaged kinetic-potential energy exchange $\bar{e}_{KtoP}^z$ for Run 3 at $t = 480\tau_0$, where quadrupole transfer structures distribute around the two box-scale structures. Figure 10(b) displays the isosurfaces of large-scale kinetic-potential energy exchange $e_{KtoP,l}$ (for $l = 2\pi/5$) for Run 3 at $t = 480\tau_0$ (the relevant buoyancy length scale is $U/N \approx 0.011$), showing quadrupole patterns around the two box-scale structures. Quadrupolar structures of different quantities are also observed in many other physical processes. Xiao *et al.* [64] found "quadrupolar" structures of the kinetic energy flux associated to strong vortices in 2D turbulence, which is similar to the quadrupolar structure of vorticity gradient stretching observed by Kimura and Herring [65]. Parashar and Matthaeus [66] also found that the current sheet formation led to generation of vorticity quadrupole in weakly collisional plasma turbulence.

The quadrupole structures near the strong vortices give rise to areas of intense e_{KtoP}, with both positive and negative values. Figure 11 depicts the average of $|e_{KtoP}|$ conditioned on Q criterion ($\langle|e_{KtoP}||Q\rangle$) and ω_z ($\langle|e_{KtoP}||\omega_z\rangle$), normalized by its spatial average in the whole domain, $\langle|e_{KtoP}|\rangle$, at different times. $|e_{KtoP}|$ is very small in regions where Q or ω_z is near zero. Moreover, $|e_{KtoP}|$ is more likely to be larger in the region with $Q > 0$ ($\omega_z > 0$) than in the region with $Q < 0$ ($\omega_z < 0$). $\langle|e_{KtoP}||Q\rangle$ and $\langle|e_{KtoP}||\omega_z\rangle$ increase significantly in time in the region with $Q > 0$ ($\omega_z > 0$), while change slightly in the region with $Q < 0$ ($\omega_z < 0$). This is consistent with the observation above that quadrupolar structures of intense kinetic-potential energy exchange are associated with strong vortices.
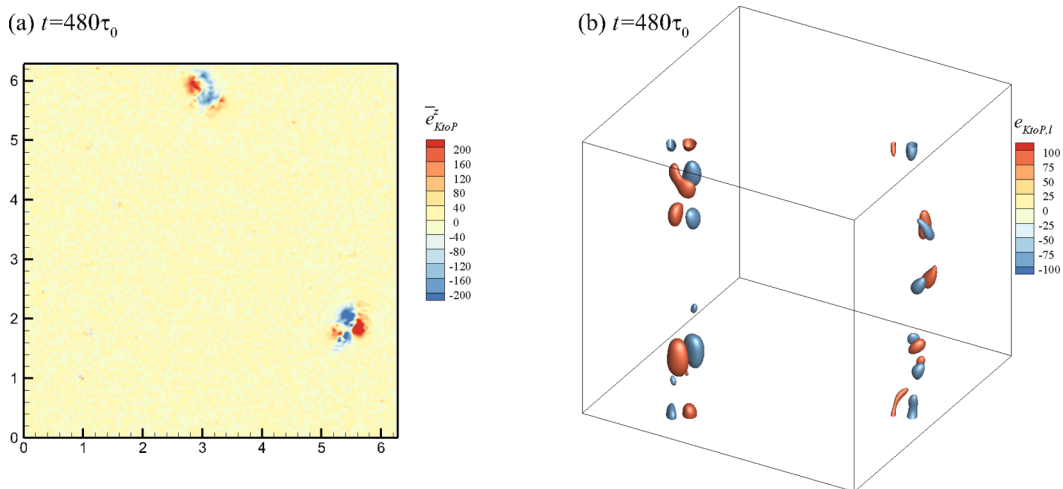
FIG. 10. (a) Vertically averaged kinetic-potential energy exchange $\bar{e}^z_{KtoP}$ and (b) isosurfaces of large-scale kinetic-potential energy exchange $e_{KtoP,l}$ (for $e_{KtoP,l} = \pm 80$), for Run 3, at $t = 480\tau_0$.

The quadrupole kinetic-potential energy exchange structures give little net contribution to the global kinetic-potential energy exchange, because of their relative rarity and the cancellation between oppositely signed exchange from the four quadrants. To show this quantitatively, we considered kinetic-potential energy exchange from regions with different values of Q and ω_z, $E_{KtoP}(Q)$, and $E_{KtoP}(\omega_z)$. Figure 12(a) shows the contribution fraction to global kinetic-potential energy exchange $E_{KtoP,t}$ from regions with different values of Q, $E_{KtoP}(Q)/E_{KtoP,t}$. Most of the contributions come from the regions where the magnitude of Q is small, and the total contribution from strain regions ($Q < 0$) is larger than that from vortex regions ($Q > 0$). Figure 12(b) shows $E_{KtoP}(\omega_z)/E_{KtoP,t}$, namely, the contribution fraction to E_{KtoP} from regions with different values of ω_z. We find that $E_{KtoP}(\omega_z)/E_{KtoP}$ is very small when $\omega_z \approx 0$. Moreover, there is one intriguing observation that $E_{KtoP}(\omega_z)/E_{KtoP}$ concentrates on the regions where $|\omega_z| < 100$, and the regions with $\omega_z < 0$ ($\omega_z > 0$) have negative (positive) $E_{KtoP}(\omega_z)/E_{KtoP,t}$. However, the total $E_{KtoP}(\omega_z)/E_{KtoP,t}$ from regions with $\omega_z < 0$ is less than that from regions with $\omega_z > 0$.

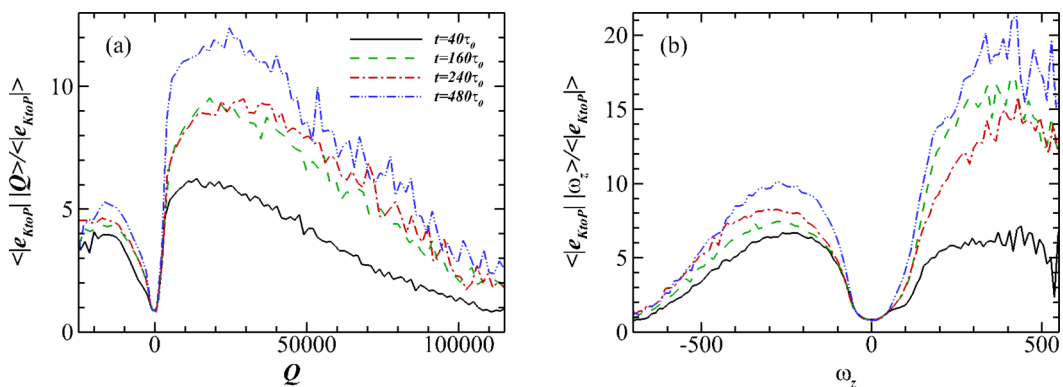FIG. 11. The average of $|e_{KtoP}|$ conditioned on (a) Q (b) ω_z, normalized by its spatial average in the whole domain, for Run 3, at different times: $40\tau_0$, black; $160\tau_0$, green; $240\tau_0$, red; $480\tau_0$, blue.
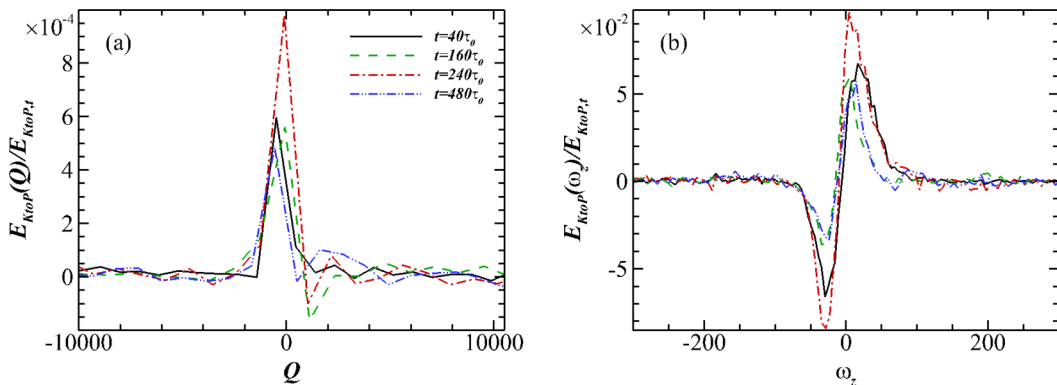
FIG. 12. The contribution fraction to global kinetic-potential energy exchange $E_{KtoP,t}$ (a) from different Q, $E_{KtoP}(Q)/E_{KtoP,t}$, and (b) from different ω_z, $E_{KtoP}(\omega_z)/E_{KtoP,t}$, for Run 3, at different times.

V. THE CONNECTION BETWEEN THE VELOCITY FIELD AND THE DENSITY FIELD

In this section, the connection between the velocity field and the density field is discussed, especially for the regions around the coherent structures. There have been many researches about this connection, including the famous thermal wind model [1,37,67,68]. However, none of them connected the velocity to density specifically around the vortices. We believe that this is important for the quasigeostrophic model which considers the dynamics principally as the interaction between vortices [41].

For our simulations with stratification, Figs. 13 and 14 show that there is a relation in vortices between the signs of ω_z and the density θ distributions at different times. Figures 13 and 14 plot the isosurfaces of Q color-coded with θ and ω_z for Run 2 and Run 3, respectively. In the cyclonic vortices with $\omega_z > 0$, θ has low values on the top while high values at the bottom, and the case is exactly opposite in the anticyclonic vortices with $\omega_z < 0$. It is worth noting that the isosurfaces of $|\omega_z|$ are quite similar to those of Q when their values are large. Therefore, ω_z has a relation with the density θ distribution in areas of large $|\omega_z|$. This is interesting because it gives the possibility of establishing a concrete relation between the velocity field $\boldsymbol{v}$ and the density field θ.

We give a heuristic explanation of the relation between the signs of ω_z and the density θ distributions in vortices. Consider the evolution of the homogeneous isotropic turbulence after the rotation and stratification are added. They act on the turbulence in the time scales $t_f = O(\text{Ro})$ and $t_N = O(\text{Fr})$, respectively. For both cases, Run 2 and Run 3, rotation acts first because $t_f < t_N$. Therefore, there should be many vertical vortex tubes in the flow field initially, as in Fig. 2(a). For a vertical vortex tube with $\omega_z > 0$, the Coriolis force F_C acts as a stretching force in the horizontal direction. The vortex tube will contract vertically because of incompressibility, accompanied with the transport of density. In consequence, compared with the background density, the density is lower on the top of the vortex tube while higher at the bottom of the vortex tube because of the stable stratification. The induced buoyancy force F_b stretches the vortex tube, balancing the contraction effect. For a vertical vortex tube with $\omega_z < 0$, the situation is an opposite to that scenario described earlier. Figure 15 shows the sketches of the vortices of both types and the forces imposed on them, where the grayscale is proportional to θ. Suppose the vortex is an incompressible deformable body, Fig. 15 indicates that only when the relation between the sign of ω_z and the density θ distribution is satisfied, the forces imposed on the vortex can balance with each other. Take Fig. 15(a) as an example, the Coriolis force exerted on a vortex with $\omega_z > 0$ stretching it horizontally. Meanwhile, $\theta > 0$ on the top and $\theta < 0$ at the bottom of the vortex, thus the induced buoyancy force stretches the vortex vertically, balancing with the Coriolis force.
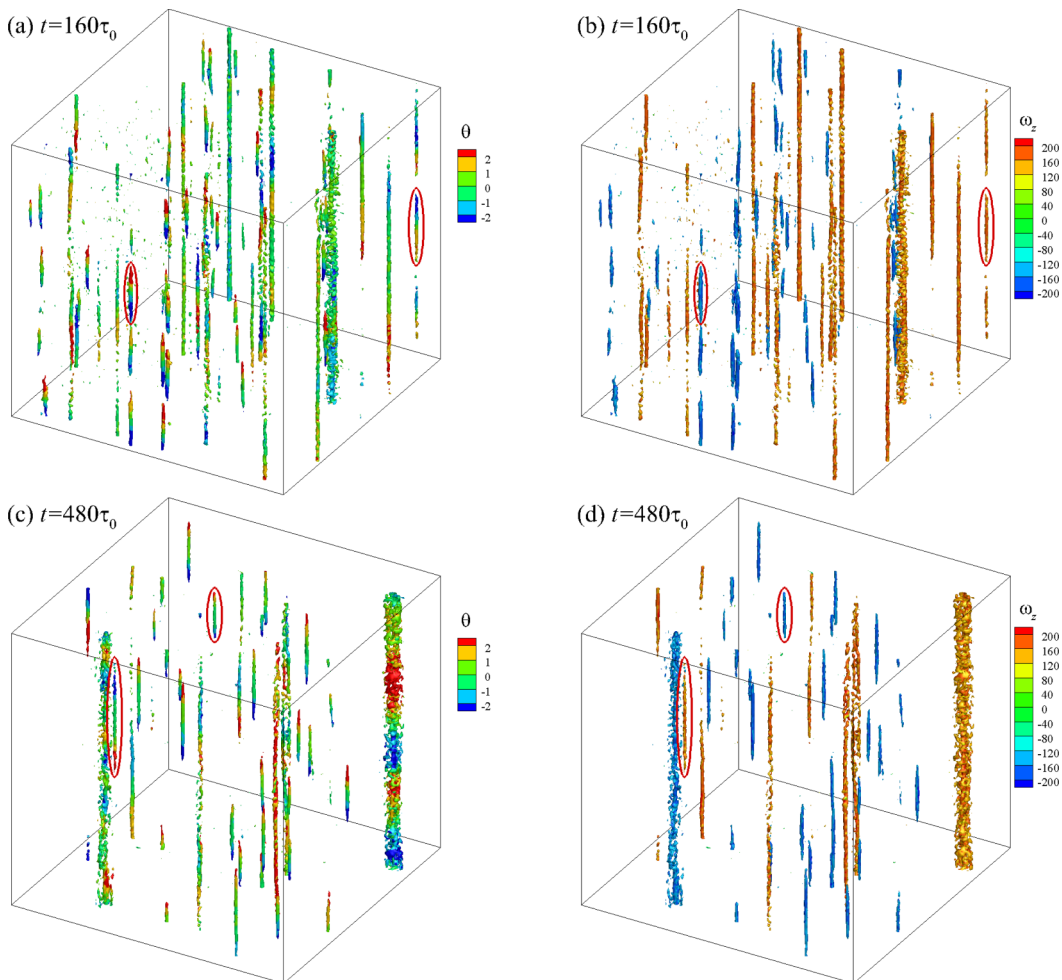
FIG. 13. Isosurfaces of Q (for $Q = 6000$) color-coded with (a)(c) density θ and (b)(d) vertical vorticity ω_z for Run 2 [(a) and (b) at $t = 160\tau_0$, (c) and (d) at $t = 480\tau_0$]. Typical vortices satisfying the relation between ω_z and the density θ distribution are circled.

Seeing that a cyclonic vortex is under tension, while an anticyclonic one is under compression, it is a natural explanation on why cyclonic vortices are easier to grow and merge with others than anticyclonic ones. Since the vortex that is under compression can easily be unstable when becoming longer (similar to the Euler buckling of a slender rod), the cyclonic vortices are less in number and larger than anticyclonic vortices, consistent with the observations about the number and volume of the two types of vortices in Sec. IV B. The formation of both types of vortices is accompanied by the positive kinetic-potential energy exchange. For vortices violating the relation between ω_z and the density θ distribution, they would be compressed (for those with $\omega_z > 0$) or broken (for those with $\omega_z < 0$) due to the imbalance of Coriolis force and buoyancy force, with negative kinetic-potential energy exchange. Such processes for vortices could be regarded as part of the primary processes of kinetic-potential energy exchange in rotating stratified turbulence.

In order to understand the relation between ω_z and the density θ distribution quantitatively, we considered the average of $\partial\theta/\partial z$ conditioned on ω_z. Figure 16(a) shows that for Run 2, $\langle\partial\theta/\partial z|\omega_z\rangle$ and ω_z have the same sign when $\omega_z > -140$, while having opposite signs when $\omega_z < -180$. This is consistent with the aforementioned relation between ω_z and θ in vortices, which implies that
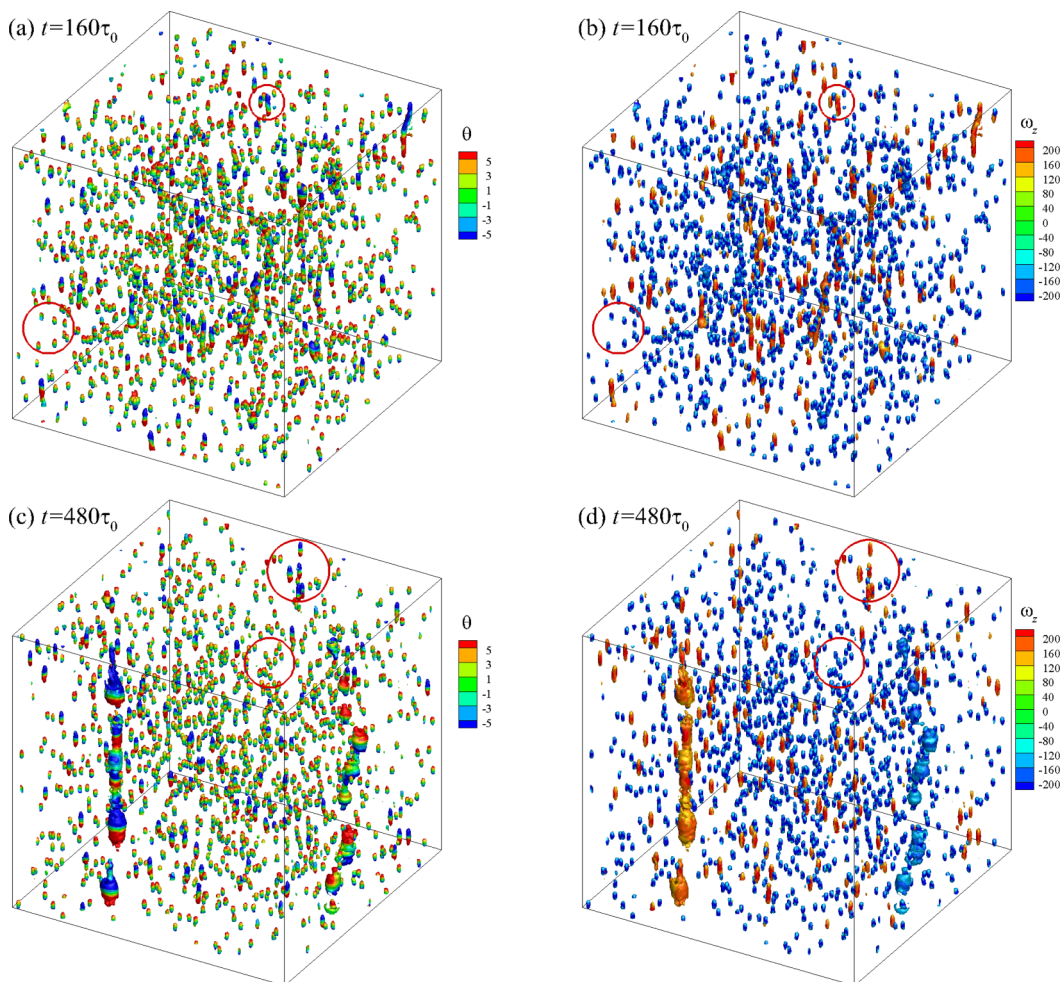
FIG. 14. Isosurfaces of Q (for $Q = 6000$) color-coded with (a) and (c) density θ and (b) and (d) vertical vorticity ω_z for Run 3 [(a) and (b) at $t = 160\tau_0$, (c) and (d) at $t = 480\tau_0$]. Typical vortices satisfying the relation between ω_z and the density θ distribution are circled.
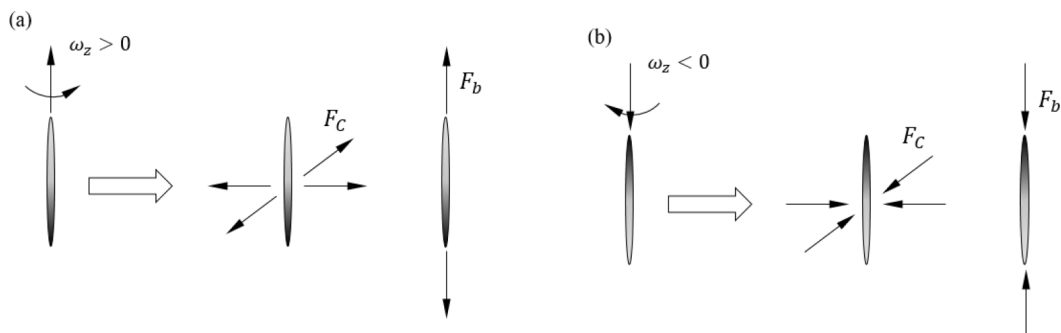

FIG. 15. Sketches of (a) a cyclonic vortex and (b) an anticyclonic vortex and the corresponding Coriolis force F_C and buoyancy force F_b imposed on them for the heuristic analysis. Note that the grayscale is proportional to θ.
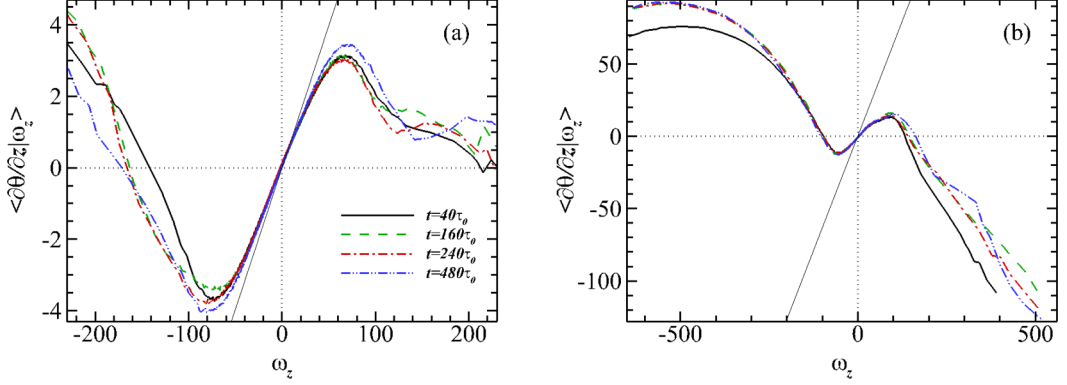
FIG. 16. The average of $\partial\theta/\partial z$ conditioned on ω_z for (a) Run 2 and (b) Run 3, at different times: $40\tau_0$, black; $160\tau_0$, green; $240\tau_0$, red; $480\tau_0$, blue. Thin solid lines have slopes of N/f for references.

$\partial\theta/\partial z$ and ω_z have opposite signs when $|\omega_z|$ is large. Moreover, $\langle\partial\theta/\partial z|\omega_z\rangle$ varies slightly over time for $|\omega_z| < 200$. The regions with $|\omega_z| < 200$ take more than 99% of the whole domain during the evolution of the turbulent system. For Run 3, Fig. 16(b) shows that $\langle\partial\theta/\partial z|\omega_z\rangle$ and ω_z have the same sign when ω_z varies approximately from -100 to 150, but they have opposite signs when the magnitude of ω_z is large. From $t = 40\tau_0$ to $t = 160\tau_0$, $\langle\partial\theta/\partial z|\omega_z\rangle$ has some noticeable differences for $\omega_z > 100$, while has negligible differences for $\omega_z < 600$ from $t = 160\tau_0$ to $t = 480\tau_0$. The regions with $\omega_z < 600$ take more than 99.99% of the whole domain during the evolution of the turbulent system. Note that near the origin, $\langle\partial\theta/\partial z|\omega_z\rangle$ has a nearly linear dependency on ω_z for both Run 2 and Run 3, which is consistent with the theory of conservation of potential vorticity [12]. In the linear limit, potential vorticity conservation reduces to

$$\frac{\partial}{\partial t}(f\hat{\mathbf{z}} \cdot \nabla\theta - N\hat{\mathbf{z}} \cdot \boldsymbol{\omega}) = 0, \tag{10}$$

from which a linear dependency $\partial\theta/\partial z \propto (N/f)\omega_z$ can be drawn. Thin solid lines with slopes of N/f are plotted in Fig. 16 for reference. Figure 16 shows that, for Run 2, the linear slope of $\langle\partial\theta/\partial z|\omega_z\rangle$ is quite close to N/f near the origin. However, for Run 3, the linear slope of $\langle\partial\theta/\partial z|\omega_z\rangle$ is far less than N/f, which is probably because the nonlinear part of the potential vorticity is not negligible and Eq. (10) is violated in the last case.

VI. CONCLUSIONS

We performed numerical simulations of forced homogeneous rotating stratified turbulence in transient state for long integration times, focusing on the flow structures and kinetic-potential energy exchange in physical space. Three simulations with a fixed Reynolds number $\mathrm{Re}_{(q)} \approx 2100$ and a low Rossby number $\mathrm{Ro} = 0.033$ are carried out with Froude numbers $\mathrm{Fr} = \infty$ (purely rotating case), 0.42, and 0.052. A constant rate of kinetic energy input ϵ_f is provided by a forcing localized at a large wave number k_f. We focus on the long-time evolution of the turbulent systems from the initial isotropic turbulence. Three main aspects of our conclusions are summarized as below.

The evolution of the flow structures for all three runs has been investigated. For the purely rotating case with $\mathrm{Ro} = 0.033$ and $\mathrm{Fr} = \infty$, slender 2D vortices dominated by cyclones spread in the whole domain, and the cyclone-anticyclone asymmetry seems to disappear at the end of the simulation as the vortices become larger and less. When stratification exists, short and small vortices fill the whole domain at the beginning, and two largest box-scale structures with opposite signs of ω_z are formed as the turbulent systems evolves. We point out the differences between the flow structures with ω_z of different signs in numbers, shapes, and evolutions. Compared to the cyclonic

vortices, anticyclonic ones are lower in number, easier to grow or merge with others, and form the box-scale structure earlier.

The kinetic-potential energy exchange e_{KtoP} is important for rotating stratified turbulence. For the case with Ro = 0.033 and Fr = 0.42, we found that there are two flow states at the early and late times, distinguished by whether the global kinetic-potential energy exchange oscillates with time or not. We investigated the structures of e_{KtoP} and their relevance with flow structures. For the case with weak stratification, Ro = 0.033 and Fr = 0.42, a box-size structure of e_{KtoP} is formed at the later flow state, which is responsible for the time oscillation of the global kinetic-potential energy exchange and associated to the condensation of a cyclonic vortex. When the strength of stratification is comparable to that of rotation, for Ro = 0.033 and Fr = 0.052, both the structures of kinetic-potential energy exchange e_{KtoP} and large-scale kinetic-potential energy exchange $e_{KtoP,l}$ have quadrupole structures. For both cases, it is remarkable that intense kinetic-potential exchange is always associated with cyclonic vortices. Note that many important destructive events in nature, such as hurricanes or typhoons, are cyclones.

We found a relation between the signs of ω_z and the distributions of density θ in vortices during the evolution of the rotating stratified turbulent systems. θ has low values on the top while high values at the bottom in cyclonic vortices, and the case is opposite in anticyclonic vortices. Heuristic explanations were introduced to illustrate this connection between the velocity field and the density field. We found that the conditional average $\langle \partial\theta/\partial z | \omega_z \rangle$ is nearly time-invariant for most part of the whole domain at later times, which could be valuable for the future modeling of density field by the velocity field.

Our current work has several limitations that are worth investigating in the future.

First, the present study has simulated cases with fixed Reynolds and Rossby numbers at various Froude numbers (Fr = ∞, 0.42 and 0.052). Varying all these parameters and comparing the results from simulations with different Reynolds and Rsossby numbers would be more informative. Note that all cases considered here have Ro < Fr, while atmospheric flows on the earth have Ro > Fr. In addition, the aspect ratio of the flow domain also influences the flow structures [12] because the existence of the rotation and stratification introduces anisotropy to the turbulence, thus it influences the kinetic-potential energy exchange as well. Therefore, the study of the effect of the aspect ratio is warranted.

The second limitation of our study is about the integration time. We have run the simulations for about 500 large eddy turnover times, which can be considered to be sufficiently long for turbulence simulations in general. Smith and Waleffe [12] showed that some flow phenomenon emerges only after a long integration time in forced rotating stratified turbulence. Considering that for 2D turbulence forced at small scale, the energy condensation could saturate and the system could reach a statistically stationary state [69]. There are possibilities for our simulations to reach stationary states after a tremendous amount of time. However, it is difficult to assess how long it takes from the end time of our simulations to the statistically stationary states, and whether our conclusions would change at later times.

Additionally, the geometry of the flow structures in rotating stratified turbulence is worth more investigating. Moisy and Jiménez [70] studied the geometry and clustering of intense structures in isotropic turbulence. In this paper, Q has been chosen as the indicator of the flow structures. Our results show that flow structures change shapes and have different distributions in the space at different conditions. A comprehensive study about the geometry of the structures should answer how geometric shapes of the structures and their distribution in the space change with the flow parameters (Re, Ro, Fr, and aspect ratio). Furthermore, we haven't discussed the structures of (kinetic and potential) energy fluxes at different scales, which are as important as those of kinetic-potential energy exchange. The energy fluxes and kinetic-potential energy exchange are associated to the evolution of the flow structures. The forms of the evolution are as following: advection, which includes inflation and shrinking, generation, vanishing, splitting and merging of the flow structures. Investigating the connections of the energy fluxes at different scales and kinetic-potential energy exchange with the change of flow structures requires us to track the flow structures in time [60,71].

Finally, please note that forced rotating stratified turbulence in transient state is investigated in this study. The steady-state regime is also very important to real atmospheric and oceanic turbulence. Stationary-state simulations have been carried out by using large scale forcing and linear damping. Preliminary results are found to be consistent with those found in the transient states, indicating our conclusions are independent of the effect of domain size or periodic boundary. More detailed analysis of the stationary states will be our future work.

[1] J. Pedlosky, *Geophysical Fluid Dynamics*, 2nd ed. (Springer, Verlag, New York, 1987).

[2] G. K. Vallis, *Atmospheric and Oceanic Fluid Dynamics* (Cambridge University Press, New York, 2017).

[3] E. Lindborg, The effect of rotation on the mesoscale energy cascade in the free atmosphere, Geophys. Res. Lett. **32**, L01809 (2005).

[4] E. Lindborg, The energy cascade in a strongly stratified fluid, J. Fluid Mech. **550**, 207 (2006).

[5] Y. Kimura and J. Herring, Energy spectra of stably stratified turbulence, J. Fluid Mech. **698**, 19 (2012).

[6] M. K. Sharma, M. K. Verma, and S. Chakraborty, On the energy spectrum of rapidly rotating forced turbulence, Phys. Fluids **30**, 115102 (2018).

[7] A. Gargett, P. Hendricks, T. Sanford, T. Osborn, and A. Williams, A composite spectrum of vertical shear in the upper ocean, J. Phys. Oceanogr. **11**, 1258 (1981).

[8] A. Gargett, T. Osborn, and P. Nasmyth, Local isotropy and the decay of turbulence in a stratified fluid, J. Fluid Mech. **144**, 231 (1984).

[9] G. Nastrom and K. S. Gage, A climatology of atmospheric wavenumber spectra of wind and temperature observed by commercial aircraft, J. Atmos. Sci. **42**, 950 (1985).

[10] J. J. Riley and M.-P. Lelong, Fluid motions in the presence of strong stable stratification, Annu. Rev. Fluid Mech. **32**, 613 (2000).

[11] O. Métais, P. Bartello, E. Garnier, J. Riley, and M. Lesieur, Inverse cascade in stably stratified rotating turbulence, Dyn. Atmos. Cceans **23**, 193 (1996).

[12] L. M. Smith and F. Waleffe, Generation of slow large scales in forced rotating stratified turbulence, J. Fluid Mech. **451**, 145 (2002).

[13] G. Hernandez-Duenas, L. M. Smith, and S. N. Stechmann, Investigation of Boussinesq dynamics using intermediate models based on wave–vortical interactions, J. Fluid Mech. **747**, 247 (2014).

[14] M. Remmel, J. Sukhatme, and L. M. Smith, Nonlinear gravity-wave interactions in stratified turbulence, Theor. Comput. Fluid Dyn. **28**, 131 (2014).

[15] H. A. Kafiabad and P. Bartello, Balance dynamics in rotating stratified turbulence, J. Fluid Mech. **795**, 914 (2016).

[16] S. B. Dalziel, Decay of rotating turbulence: Some particle tracking experiments, Appl. Sci. Res. **49**, 217 (1992).

[17] O. Zeman, A note on the spectra and decay of rotating homogeneous turbulence, Phys. Fluids **6**, 3221 (1994).

[18] Y. Zhou, A phenomenological treatment of rotating turbulence, Phys. Fluids **7**, 2092 (1995).

[19] A. Babin, A. Mahalov, and B. Nicolaenko, Global splitting, integrability and regularity of 3D Euler and Navier-Stokes equations for uniformly rotating fluids, Eur. J. Mech. B **15**, 291 (1996).

[20] P. Bartello, O. Métais, and M. Lesieur, Coherent structures in rotating three-dimensional turbulence, J. Fluid Mech. **273**, 1 (1994).

[21] C. Cambon, N. N. Mansour, and F. S. Godeferd, Energy transfer in rotating turbulence, J. Fluid Mech. **337**, 303 (1997).

[22] L. M. Smith and F. Waleffe, Transfer of energy to two-dimensional large scales in forced, rotating three-dimensional turbulence, Phys. Fluids **11**, 1608 (1999).

[23] F. Waleffe, The nature of triad interactions in homogeneous turbulence, Phys. Fluids A **4**, 350 (1992).

[24] F. Waleffe, Inertial transfers in the helical decomposition, Phys. Fluids A **5**, 677 (1993).

[25] Q. Chen, S. Chen, G. L. Eyink, and D. D. Holm, Resonant interactions in rotating homogeneous three-dimensional turbulence, J. Fluid Mech. **542**, 139 (2005).

[26] J. R. Herring and O. Métais, Numerical experiments in forced stably stratified turbulence, J. Fluid Mech. **202**, 97 (1989).

[27] O. Métais and M. Lesieur, Spectral large-eddy simulation of isotropic and stably stratified turbulence, J. Fluid Mech. **239**, 157 (1992).

[28] G. Brethouwer, P. Billant, E. Lindborg, and J.-M. Chomaz, Scaling analysis and simulation of strongly stratified turbulent flows, J. Fluid Mech. **585**, 343 (2007).

[29] F. S. Godeferd and C. Cambon, Detailed investigation of energy transfers in homogeneous stratified turbulence, Phys. Fluids **6**, 2084 (1994).

[30] M. L. Waite and P. Bartello, Stratified turbulence dominated by vortical motion, J. Fluid Mech. **517**, 281 (2004).

[31] R. Marino, P. D. Mininni, D. Rosenberg, and A. Pouquet, Emergence of helicity in rotating stratified turbulence, Phys. Rev. E **87**, 033016 (2013).

[32] W. J. McKiver and D. G. Dritschel, Balance in non-hydrostatic rotating stratified turbulence, J. Fluid Mech. **596**, 201 (2008).

[33] G. Roullet and P. Klein, Available potential energy diagnosis in a direct numerical simulation of rotating stratified turbulence, J. Fluid Mech. **624**, 45 (2009).

[34] C. Ménesguen, B.-L. Hua, C. Papenberg, D. Klaeschen, L. Geli, and R. Hobbs, Effect of bandwidth on seismic imaging of rotating stratified turbulence surrounding an anticyclonic eddy from field data and numerical simulations, Geophys. Res. Lett. **36**, L00D05 (2009).

[35] C. Garrett, P. MacCready, and P. Rhines, Boundary mixing and arrested Ekman layers: Rotating stratified flow near a sloping boundary, Annu. Rev. Fluid Mech. **25**, 291 (1993).

[36] P. Bartello, Geostrophic adjustment and inverse cascades in rotating stratified turbulence, J. Atmos. Sci. **52**, 4410 (1995).

[37] H. Hanazaki, Linear processes in stably and unstably stratified rotating turbulence, J. Fluid Mech. **465**, 157 (2002).

[38] R. Marino, P. D. Mininni, D. Rosenberg, and A. Pouquet, Inverse cascades in rotating stratified turbulence: Fast growth of large scales, Europhys. Lett. **102**, 44006 (2013).

[39] J. C. McWilliams, J. B. Weiss, and I. Yavneh, Anisotropy and coherent vortex structures in planetary turbulence, Science **264**, 410 (1994).

[40] J. N. Reinaud and D. G. Dritschel, The merger of vertically offset quasi-geostrophic vortices, J. Fluid Mech. **469**, 287 (2002).

[41] J. N. Reinaud, D. G. Dritschel, and C. Koudella, The shape of vortices in quasi-geostrophic turbulence, J. Fluid Mech. **474**, 175 (2003).

[42] C. Cambon, Turbulence and vortex structures in rotating and stratified flows, Eur. J. Mech. **20**, 489 (2001).

[43] L. Liechtenstein, F. S. Godeferd, and C. Cambon, Nonlinear formation of structures in rotating stratified turbulence, J. Turbul. **6**, N24 (2005).

[44] E. Itsweire, K. Helland, and C. Van Atta, The evolution of grid-generated turbulence in a stably stratified fluid, J. Fluid Mech. **162**, 299 (1986).

[45] C. Van Atta *et al.*, The decay of turbulence in thermally stratified flow, J. Fluid Mech. **210**, 57 (1990).

[46] K. Yoon and Z. Warhaft, The evolution of grid-generated turbulence under conditions of stable thermal stratification, J. Fluid Mech. **215**, 601 (1990).

[47] D. Ramsden and G. Holloway, Energy transfers across an internal wave-vortical mode spectrum, J. Geophys. Res.: Oceans **97**, 3659 (1992).

[48] E. Deusebio, A. Vallgren, and E. Lindborg, The route to dissipation in strongly stratified and rotating flows, J. Fluid Mech. **720**, 66 (2013).

[49] B. T. Nadiga, Nonlinear evolution of a baroclinic wave and imbalanced dissipation, J. Fluid Mech. **756**, 965 (2014).

[50] H. A. Kafiabad and P. Bartello, Spontaneous imbalance in the non-hydrostatic Boussinesq equations, J. Fluid Mech. **847**, 614 (2018).

[51] A. Lozano-Durán, O. Flores, and J. Jiménez, The three-dimensional structure of momentum transfer in turbulent channels, J. Fluid Mech. **694**, 100 (2012).

[52] A. Perry and M. Chong, Topology of flow patterns in vortex motions and turbulence, Appl. Sci. Res. **53**, 357 (1994).

[53] E. Yarom, Y. Vardi, and E. Sharon, Experimental quantification of inverse energy cascade in deep rotating turbulence, Phys. Fluids **25**, 085105 (2013).

[54] A. Campagne, B. Gallet, F. Moisy, and P.-P. Cortet, Direct and inverse energy cascades in a forced rotating turbulence experiment, Phys. Fluids **26**, 125112 (2014).

[55] L. M. Polvani, J. McWilliams, M. Spall, and R. Ford, The coherent structures of shallow-water turbulence: Deformation-radius effects, cyclone/anticyclone asymmetry and gravity-wave generation, Chaos **4**, 177 (1994).

[56] G. Roullet and P. Klein, Cyclone-Anticyclone Asymmetry in Geophysical Turbulence, Phys. Rev. Lett. **104**, 218501 (2010).

[57] F. Moisy, C. Morize, M. Rabaud, and J. Sommeria, Decay laws, anisotropy and cyclone–anticyclone asymmetry in decaying rotating turbulence, J. Fluid Mech. **666**, 5 (2011).

[58] B. Gallet, A. Campagne, P.-P. Cortet, and F. Moisy, Scale-dependent cyclone-anticyclone asymmetry in a forced rotating turbulence experiment, Phys. Fluids **26**, 035108 (2014).

[59] O. Praud, J. Sommeria, and A. M. Fincham, Decaying grid turbulence in a rotating stratified fluid, J. Fluid Mech. **547**, 389 (2006).

[60] A. Lozano-Durán and J. Jiménez, Time-resolved evolution of coherent structures in turbulent channels: Characterization of eddies and cascades, J. Fluid Mech. **759**, 432 (2014).

[61] K. L. Chong, Y. Yang, S.-D. Huang, J.-Q. Zhong, R. J. Stevens, R. Verzicco, D. Lohse, and K.-Q. Xia, Confined Rayleigh-Bénard, Rotating Rayleigh-Bénard, and Double Diffusive Convection: A Unifying View on Turbulent Transport Enhancement through Coherent Structure Manipulation, Phys. Rev. Lett. **119**, 064501 (2017).

[62] M. Germano, Turbulence: The filtering approach, J. Fluid Mech. **238**, 325 (1992).

[63] K. L. Chong, S.-D. Huang, M. Kaczorowski *et al.*, Condensation of Coherent Structures in Turbulent Lows, Phys. Rev. Lett. **115**, 264503 (2015).

[64] Z. Xiao, M. Wan, S. Chen, and G. Eyink, Physical mechanism of the inverse energy cascade of two-dimensional turbulence: A numerical investigation, J. Fluid Mech. **619**, 1 (2009).

[65] Y. Kimura and J. R. Herring, Gradient enhancement and filament ejection for a non-uniform elliptic vortex in two-dimensional turbulence, J. Fluid Mech. **439**, 43 (2001).

[66] T. N. Parashar and W. H. Matthaeus, Propinquity of current and vortex structures: Effects on collisionless plasma heating, Astrophys. J. **832**, 57 (2016).

[67] O. Métais and J. R. Herring, Numerical simulations of freely evolving turbulence in stably stratified fluids, J. Fluid Mech. **202**, 117 (1989).

[68] O. Iida and Y. Nagano, Coherent structure and heat transfer in geostrophic flow under density stratification, Phys. Fluids **11**, 368 (1999).

[69] C.-k. Chan, D. Mitra, and A. Brandenburg, Dynamics of saturated energy condensation in two-dimensional turbulence, Phys. Rev. E **85**, 036315 (2012).

[70] F. Moisy and J. Jiménez, Geometry and clustering of intense structures in isotropic turbulence, J. Fluid Mech. **513**, 111 (2004).

[71] J. I. Cardesa, A. Vela-Martín, and J. Jiménez, The turbulent cascade in five dimensions, Science **357**, 782 (2017).